JACS
JOURNAL OF THE AMERICAN CHEMICAL SOCIETY
Article
pubs.acs.org/JACS

Carbon Monoxide-Assisted Synthesis of Single-Crystalline Pd Tetrapod Nanocrystals through Hydride Formation

Yan Dai,[†] Xiaoliang Mu,[†] Yueming Tan,[†] Kaiqiang Lin,[†] Zhilin Yang,[‡] Nanfeng Zheng,*[,†] and Gang Fu*[,†]

[†]State Key Laboratory for Physical Chemistry of Solid Surfaces and Department of Chemistry, College of Chemistry and Chemical Engineering, Xiamen University, Xiamen 361005, China

[‡]Department of Physics, Xiamen University, Xiamen 361005, China

Supporting Information

ABSTRACT: Carbon monoxide can adsorb specifically on Pd(111) to induce the formation of unique Pd nanostructures. In the copresence of CO and H_2, single-crystalline Pd tetrapod nanocrystals have now been successfully prepared. The Pd tetrapods are enclosed by (111) surfaces and are yielded through hydride formation. Density functional theory calculations revealed that the formation of PdH_x in the presence of H_2 reduces the binding energy of CO on Pd and thus helps to decrease the CO coverage during the synthesis, which is essential to the formation of the PdH_x tetrapod nanocrystals. In addition to tetrapod nanocrystals, tetrahedral nanocrystals were also produced in the copresence of CO and H_2 when the reaction temperature was ramped to further lower the CO coverage. Upon aging in air, the as-prepared PdH_x nanocrystals exhibited a shape-dependent hydrogen releasing behavior. The conversion rate of PdH_x tetrapod nanocrystals into metallic Pd was faster than that of tetrahedral nanocrystals.

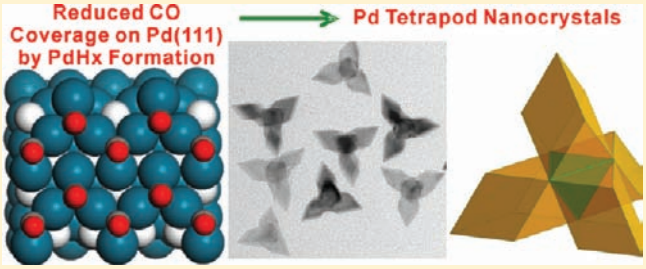

INTRODUCTION

The properties of noble metal nanocrystals are highly determined by their size, shape, and surface structures.[1−3] The controlled synthesis of noble metal nanocrystals has thus attracted increasing research attention, with the aim of tailoring their properties for applications in devices, photonics, sensing, and catalysis.[1−3] In the past decades, a number of synthetic strategies have been developed to control the morphology of noble metal nanocrystals.[2−5] For Pd and Pt nanocrystals, more recently, the strong and specific surface adsorption of small adsorbates has emerged as a power strategy to control the surface structure of their nanocrystals.[6−15] For instance, the preferential adsorption of halides on Pd{100} promotes the formation of Pd nanocubes enclosed by Pd{100} facets.[9,10] The coadsorption of CO and amines makes Pt{100} more energetically stable than Pt{111} and thus induces the formation of Pt nanocubes.[11,13] CO prefers to adsorb on Pd{111} surface and facilitates the growth of ultrathin Pd nanosheets having {111} as the main exposure surface and displaying unique optical properties.[12,16] The adsorption of methylamine stabilizes the stepped sites and therefore assists the formation of Pt octapods enclosed by {411} facets exhibiting extraordinary electrocatalytic properties.[14]

Although, for face-centered cubic (fcc) metals, the morphology and surface of their nanocrystals are closely related issues, their properties depend differently upon the morphology and surface structure of the nanocrystals.[2−4,17] For example, as a surface property, catalysis of noble metal nanocrystals concerns more of their surface structure.[2,18,19] In contrast, the surface plasmon resonance (SPR) properties of noble metal nanocrystals are more sensitive to their morphology rather than exposure surfaces.[20−24] Since the specific adsorption of small adsorbates controls only the surface structure of Pd and Pt nanocrystals, other factors beyond the specific adsorption have been utilized to enrich the morphology of noble metal nanocrystals. Two recent examples are (1) the preferential growth of micrometer-long five-fold twinned Pd nanowires over Pd nanocubes under slow reduction in the presence of I^-,[25] and (2) the production of corolla-like Pd mesocrystals in the copresence of Fe^{3+} as the oxidative etchant and CO as the surface controller.[16] In these two examples, the control over the reduction kinetics and introducing oxidative etching to disturb the growth of seeds enrich the morphology of noble metal nanocrystals. However, the question remains whether there are further avenues to enrich the shape of nanocrystals in the presence of specific strong surface adsorbate.

Herein, we now demonstrate that, while CO specifically adsorbs on Pd(111), the adsorption strength and coverage of CO on Pd can be essentially varied by introducing H_2 to facilitate the formation of single-crystalline Pd tetrapod and tetrahedral nanocrystals enclosed by (111) surfaces. In the copresence of CO and H_2, the freshly prepared tetrapod and tetrahedral nanocrystals were β-PdH_x but not pure Pd nanocrystals. Upon aging in air, the as-prepared β-PdH_x

Received: January 19, 2012
Published: April 3, 2012

   dx.doi.org/10.1021/ja3006429 | J. Am. Chem. Soc. 2012, 134, 7073−7080

nanocrystals released hydrogen and were converted gradually to Pd nanocrystals. As revealed by density functional theory (DFT) calculations, the formation of palladium hydride in the presence of H_2 weakens the chemisorption of CO and therefore helps to lower the CO coverage to induce the formation of Pd tetrapod nanocrystals.

EXPERIMENTAL SECTION

Chemicals and Materials. Palladium(II) acetylacetonate [Pd-(acac)$_2$] (99%) was purchased from Alfa Aesar. Poly(vinylpyrrolidone) (PVP, MW = 58 000, AR), tetrabutylammonium bromide (TBAB), and *N*,*N*-dimethylformamide (DMF) were purchased from Sinopharm Chemical Reagent Co. Ltd. (Shanghai, China). Pd black was purchased from Aldrich Chemical Co. All reagents were used as received without further purification.

Synthesis of Pd Tetrapod Nanocrystals. In a typical synthesis of Pd tetrapod nanocrystals, 10 mg of Pd (acac)$_2$, 90 mg of PVP were dissolved in 10 mL of DMF. The resulting homogeneous solution was transferred to a glass pressure vessel. After being charged with CO:H_2 = 1:4 to 2 bar, the vessel was heated from room temperature to 100 °C in 20 min and kept at this temperature for another 160 min with stirring. The resulting products were collected by centrifugation and washed several times with ethanol and acetone.

Synthesis of Pd Tetrahedral Nanocrystals. In 10 mL of DMF, 10 mg of Pd (acac)$_2$ and 90 mg of PVP were dissolved. The resulting homogeneous solution was transferred to a glass pressure vessel. After being charged with CO:H_2 = 1:4 to 2 bar, the vessel was heated from room temperature to 140 °C in 20 min and kept at this temperature for another 160 min with stirring. The resulting products were collected by centrifugation and washed several times with ethanol and acetone.

Synthesis of Pd Nanosheet Seeds. With DMF (10 mL) and water (2 mL), 50.0 mg of Pd(acac)$_2$, 160.0 mg of PVP, and 161 mg of TBAB were mixed together. The resulting homogeneous solution was transferred to a glass pressure vessel. The vessel was then charged with CO to 1 bar and heated at 70 °C for 4.0 h before it was cooled to room temperature.

Seeded Growth of Pd Nanosheets. In 2 mL of DMF, a 2 mL solution of the above nanosheet seeds were washed once and dispersed. The seed solution was then mixed with an 8 mL DMF solution containing 32 mg of Pd(acac)$_2$. The resulting homogeneous solution was transferred to a glass pressure vessel. After being charged with CO or H_2 to 1 bar or CO/H_2 (1:4) mixture to 2 bar, the vessel was heated at 60 °C for 2.0 h with stirring for the seeded growth.

Characterization. TEM (including high-resolution transmission electron microscope, HRTEM) studies were performed on a TECNAI F-30 high-resolution transmission electron microscope operating at 300 kV. The samples were prepared by dropping ethanol dispersion of samples onto 300-mesh carbon-coated copper grids and immediately evaporating the solvent. The powder X-ray diffraction (XRD) measurements were performed with an X'pert PRO instrument (PANalytical) using Cu Kα radiation (λ = 0.15418 nm). The thicknesses of nanosheets were measured by supporting the nanosheets on carbon nanotubes.

Electrochemical Measurements. Ethanol dispersion of purified nanoparticles was deposited on a glassy carbon electrode to obtain the working electrodes after the solvent is dried by an IR lamp. A saturated calomel electrode (SCE) and a platinum foil were used as the reference and counter electrode, respectively. For the CO stripping voltammetry measurements, CO gas (99.99%) was bubbled at an open circuit for 15 min through 0.1 M H_2SO_4 solution in which the electrode immersed. The electrode was quickly moved to a fresh solution, and the CO stripping voltammetry was recorded at a sweep rate of 2 mV/s.

For the electro-oxidation of formic acid, the cyclic voltammograms were recorded at a sweep rate of 50 mV/s in 0.5 M H_2SO_4 + 0.25 M formic acid. Before cyclic voltammetry (CV) measurements, two cycles of potential sweeps between −0.25 and 1.2 V at a sweep rate of 250 mV/s were applied. The current is normalized by the electrochemically active surface areas (ECSA) of catalysts in the electrode, which was estimated from the integrated reduction charge of surface palladium oxide by assuming a charge of 424 μC/cm^2 for the reduction of palladium oxide monolayer.[26] The Pd contents in the electrode were quantitatively analyzed by inductively coupled plasma. To test the stability of the catalysts in the electro-oxidation of formic acid, the cyclic voltammograms were recorded at a sweep rate of 200 mV/s in 0.5 M H_2SO_4 + 0.25 M formic acid, between −0.2 and 0.8 V (vs SCE) for 100 cycles.

Catalysis. Catalytic hydrogenation of styrene was carried out in a well-stirred glass pressure vessel (75 mL) at 40 °C. Dispersed in 10 mL ethanol, 0.5 mg of the catalysts (i.e., Pd tetrapod nanocrystals and Pd black) were mixed with 20 mmol (2.3 mL) styrene in the pressure vessel. H_2 flow was applied into the vessel for several minutes to remove oxygen. The vessel was then pressurized by 2.0 bar H_2. The reaction was allowed to proceed, and samples were withdrawn at regular intervals, filtered, and analyzed by gas chromatography (GC) and gas chromatography−mass spectrometry (GC−MS).

Computational Details. Periodic DFT calculations were carried out with the Vienna ab initio simulation package (VASP).[27,28] The electron exchange and correlation were treated within the generalized gradient approximation using the Perdew, Burke, and Ernzerhof (PBE) functional.[29] The projector augmented plane wave (PAW) method was used for describing electron−ion interactions, with an energy cutoff of 400 eV.[30,31] The convergence criteria for the energy calculation and structure optimization were set to a self-consistent field (SCF) tolerance of 1.0×10^{-4} eV and a maximum Hellmann−Feynman force tolerance of 0.01 eV/Å.

The CO-Pd(111) system has been extensively studied over the past 20 years. Experimentally, a set of ordered CO adsorption patterns have been determined.[32,33] In addition, CO adsorption on Pd surfaces was also a subject of much theoretical work.[34−36] Three key modes,[32−34] such as, $\sqrt{3} \times \sqrt{3}$ R30° (0.33 ML), C(4 × 2)-2CO (0.50 ML) and C(2 × 2)-3CO (0.75 ML), were considered in our calculations. The Pd(111) surface was modeled by five-layer slabs with different supper-lattice sizes, i.e., $\sqrt{3} \times \sqrt{3}$, C(4 × 2), and C(2 × 2). During structural optimization, the bottom two layers were fixed at bulk truncated position, while the top three layers and CO were fully relaxed. The *k*-points sampling was generated following the Monkhorst−Pack procedure with a 7 × 7 × 1 mesh for $\sqrt{3} \times \sqrt{3}$ R30° while 5 × 5 × 1 mesh for C(4 × 2)-2CO and C(2 × 2)-3CO.

CO−H interaction on Pd(111) surface has also attracted much attention.[37−40] The main conclusion is that CO coadsorption will cause adsorbed H atoms desorbing as H_2 or dissolving into Pd lattice. Morkel et al. further pointed that for Pd nanoparticles, a hydride phase is more easily formed, and dissolved hydrogen starts to desorb only after a considerable amount of CO has been removed.[37] All these indicated that the β-PdH$_x$ phase should be relatively stable under our synthesis condition. According to the neutron diffraction experiment,[41,42] H atoms locate on the octahedral position in the bulky Pd lattice, with a saturation concentrate of $x \approx 0.64$. For simplicity, we assume that all octahedral sites are occupied by H atoms, giving an ideal monohydride PdH. The computational parameters for CO/PdH(111) system are similar to those for CO/Pd(111). At the level of PBE/PAW, our calculation showed that the lattice constant is expanded by 4%, from 3.936 to 4.091 Å (bulk Pd and PdH, respectively), consistent with experimental observations. The adsorption energies for CO on Pd(111) and PdH(111) at different coverages are listed in Table 1. The average adsorption energy $\overline{\Delta E_{ads}}$ is defined as follows:

$$\overline{\Delta E_{ads}} = \Delta E_{ads}/n \quad (1)$$

with

$$\Delta E_{ads} = E(\text{slab}/n{\cdot}\text{CO}) - E(\text{slab}) - n{\cdot}E(\text{CO}) \quad (2)$$

in which E(slab/CO) is the energy of the slab with CO adlayer; E(slab) stands for the energy of the slab, and E(CO) the energy of CO in the gas phase. And n is the number of adsorbed CO in one unit cell.

dx.doi.org/10.1021/ja3006429 | J. Am. Chem. Soc. 2012, 134, 7073−7080

To elucidate the influences of palladium hydride formation on the growth mechanism of Pd tetrapod nanocrystal, we further consider following equilibrium:

$$\text{surface} + n_{ads}\text{CO(gas)} \leftrightarrow [\text{surface} - n_{ads}\text{CO}] \quad (3)$$

The related Gibbs free energy in one unit cell at a given temperature and CO pressure is[43,44]

$$\Delta G_{ads} = G(\text{surface} - n_{ads}\text{CO, solid}) - G(\text{surface, solid}) - n_{ads}\mu(\text{CO, gas}) \quad (4)$$

The solid Gibbs free energies and gas phase chemical potential can be written as

$$G(\text{solid}) = H_0 - RT\ln(Q_{vib}) \quad (5)$$

$$\mu(\text{gas}) = H_0 - RT\ln(Q_{vib}\cdot Q_{rot}\cdot Q_{trans}) + RT \quad (6)$$

where

$$H_0 = E_{el} + E_{ZPE} \quad (7)$$

Here H_0 is the enthalpy at 0 K, which is equal to total electronic energy (E_{el}) plus the zero point correction energy (E_{ZPE}), and Q_{vib}, Q_{rot}, and Q_{trans} are the partition functions for vibrations, rotations, and translations. Additionally, RT replaces the volume work of ideal gas. For gas phase molecule, these data can be obtained by using Gaussian03 code.[45] In this case, PBE functional combined with Dunning's correlation consistent basis set, cc-pVQZ, is employed.[29,46] Here, we neglect the internal vibrational contribution of solid and assume that both E_{ZPE} and $RT\ln Q_{vib}$ are the same whenever CO is in gas phase or adsorbed on the surface. Accordingly, eq 4 can be rewritten as

$$\Delta G_{ads} = \Delta E_{ads} - n\cdot(-RT\ln Q_{rot}(\text{CO, gas}) - RT\ln Q_{trans}(\text{CO, gas}) + RT) \quad (8)$$

Finally, surface free energy can be obtained by

$$\phi = \Delta G_{ads}/N_{surf} \quad (9)$$

where N_{surf} stands for the number of surface Pd atoms in the slab.

According to eq 9 and the Boltzmann distribution, the concentration and types of CO adsorption patterns on the Pd(111) and PdH(111) can be estimated.

RESULTS AND DISCUSSION

Structure of Pd Tetrapod Nanocrystals. The representative electron microscopic images of the as-made Pd nanocrystals are illustrated in Figure 1 and Supporting Information. It was clearly revealed that tetrapod Pd nanocrystals were the dominant products. Both the selected area electron diffraction (SAED) and HRTEM measurements on a single tetrapod clearly indicate their single-crystalline nature. The HRTEM image (Figure 1c) of the tetrapod nanocrystals shows lattice fringes with an interplanar spacing of 0.195 nm, corresponding to {200} planes of fcc Pd. The SAED pattern (Figure 1d) of an individual tetrapod Pd nanocrystal (inset of Figure 1c) contains spots from an fcc structure viewed down the ⟨100⟩ zone axis. Based on the observed TEM images, we proposed a geometric model for the as-made Pd tetrapod nanocrystals.

In the proposed model (Figure 2a), four rhombohedra are jointed together by sharing one tetrahedron at the center to form the tetrapod. As illustrated in Figure 2b, each rhombohedron is enclosed by six rhombus-like {111} faces. Sharing one tetrahedron at the center drives the four rhombohedra together to the concave tetrahedron structure. Overall, an ideal tetrapod nanocrystals consists of 12 rhombus-like {111} faces and also 12 regular triangular {111} faces. All exposure surfaces for the tetrapods are {111} facets. A set of tilted TEM images (Figure S2, Supporting Information) of the tetrapod nanocrystals were taken to verify the proposed

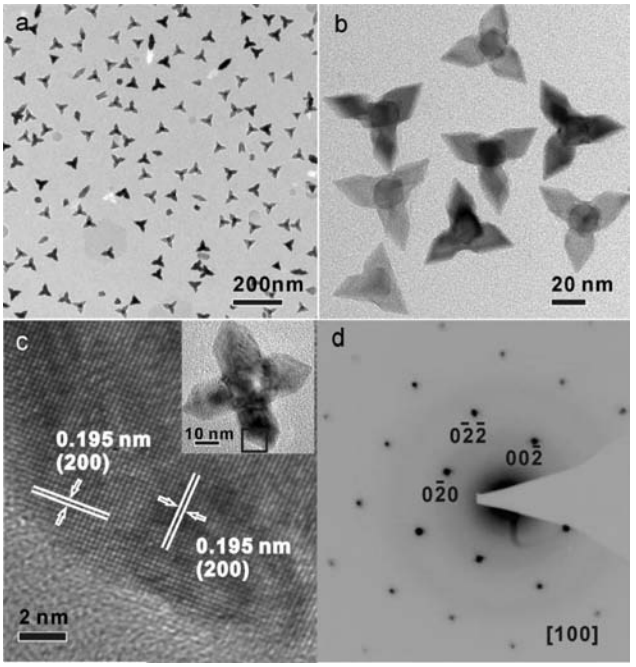

Figure 1. (a) Large-area and (b) enlarged TEM images of as-synthesized Pd nanocrystals. (c) HRTEM image of an individual Pd tetrapod nanocrystal oriented along the ⟨100⟩ direction (inset) and (d) its corresponding SAED pattern.

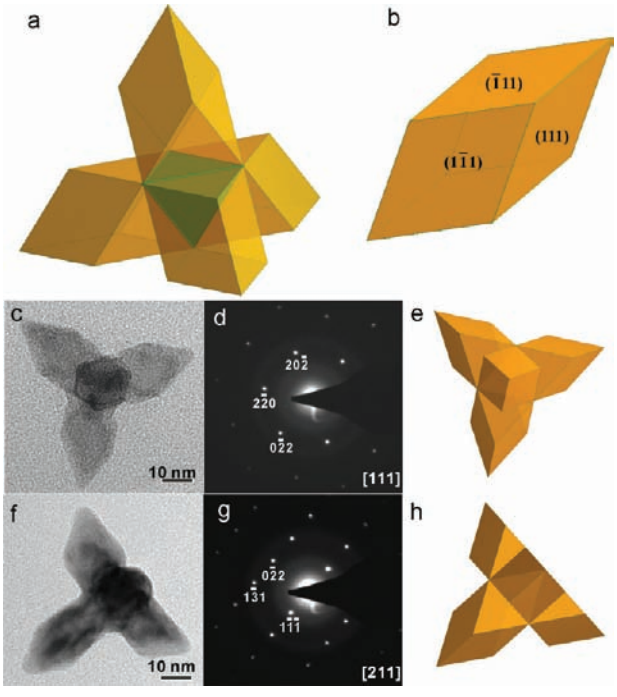

Figure 2. (a) An ideal 3D geometrical model of a tetrapod nanocrystal. (b) Model of one rhombohedral arm of the tetrapod. (c,f) TEM images, (d,g) SAED patterns, and (e,h) geometric models of an individual Pd tetrapod nanocrystals oriented along the (c–e) [111] and (f–h) [211] directions.

dx.doi.org/10.1021/ja3006429 | J. Am. Chem. Soc. 2012, 134, 7073–7080

structure model. For individual tetrapod nanocrystals oriented along [111] or [211] zone axis, their TEM images and SAED patterns also match well with the corresponding geometric models (Figure 2c–h). The presence of {111} exposure surface in the as-prepared tetrapod nanocrystals was also confirmed by the CO stripping experiments in H_2SO_4 solution. The main peak observed in the CO stripping curve of the Pd tetrapods (Figure S3, Supporting Information) is indeed attributed to the CO stripping on Pd(111) facet.[47]

Based on the above structural dissection, one should be aware that the tetrapod structure reported here significantly differs from those previously reported. So far, the reported tetrapod structures were mainly limited to II–VI semiconductors (e.g., CdSe, CdS, MnS, CdTe, ZnTe, ZnS, ZnO).[48−51] A number of studies have revealed that these compositions can be used to fabricate tetrapod structure because they have both cubic (zinc blend) and hexagonal (wurtzite) phases. While the cubic structure is important to create the core having four active sites for growth of four arms, the hexagonal structure is essential to the anisotropic growth of each arm. In comparison with II–VI semiconductors, the tetrapods reported here are single-crystalline nanocrystals made of fcc Pd. Although single-crystalline Au tetrapod nanocrystals were observed,[52] the Pd tetrapod reported here represents a new type of morphology having {111} as exposure surfaces.

Formation Mechanism of Pd Tetrapod Nanocrystals. To better understand how the tetrapod Pd nanocrystals were produced in our system, the intermediate Pd nanocrystals yielded at different reaction times were investigated by TEM (Figure 3). The Pd tetrapod produced in a 30 min reaction had

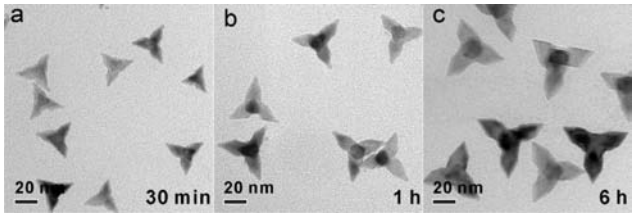

Figure 3. TEM images of the Pd tetrapod nanocrystals produced at (a) 30 min, (b) 1.0 h, and (c) 6.0 h.

a side length (tip-to-tip distance) of ~35 nm. These nanocrystals continued to grow within 3 h. Their average side length was increased to 51 nm at 1 h and 60 nm at 3 h (Figure 1b). The tetrapod feature readily appeared at 30 min and became more and more obvious with the size enlargement as the reaction proceeded. The tetrapod feature of the nanocrystals became evident after 1 h. No further change on both the size and the morphology of the nanocrystals was observed beyond 3 h. These results imply that the concave feature of the Pd tetrapod is not produced by etching, although etching has been demonstrated as an effective method to create branched noble metal nanostructures.[16]

In the synthesis of Pd tetrapods, the copresence of CO and H_2 is essential. No Pd tetrapods were obtained in absence of either CO or H_2 (Figure S4, Supporting Information). While the absence of CO produced Pd nanoaggregates with ill-defined structure, the absence of H_2 yielded ultrathin Pd nanosheets. In the presence of pure CO, as demonstrated in our previous studies, the production of ultrathin Pd nanosheets having (111) as the dominating exposed surface is mainly due to the strong and preferential chemisorption of CO on Pd(111).[12] Under the strong surface confinement effect of CO, ultrathin nanosheets are selectively produced because they have more growth active sites to fight against the CO confinement and therefore are more favored by growth kinetics. However, due to their ultrathin feature, the exposed surface area of the nanosheets increases linearly with volume. The Pd nanosheets are not thermodynamically stable products. Why were Pd tetrapods yielded only when H_2 was introduced together with CO? We believe that such a H_2 effect is induced by the modified chemisorption property of CO on Pd(111) in the presence of H_2.

It is well-known that metallic Pd is catalytically active to split H_2 molecules to hydrogen atoms which can exclusively permeate into Pd to form metal hydride.[53−55] Although our TEM studies revealed that all detected tetrapods were metallic Pd, one should not exclude the possibility that the observed Pd nanostructures were converted from palladium hydrides, particularly under the high-vacuum conditions. In fact, the powder XRD measurements (Figure 4) on the freshly prepared

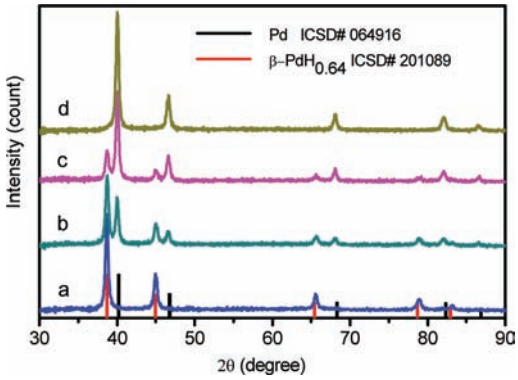

Figure 4. XRD patterns of Pd tetrapod nanocrystals: (a) freshly prepared samples and after being aged in air for (b) 9, (c) 18, and (d) 63 min.

Pd nanocrystals confirmed that the as-prepared tetrapods were β-PdH_x but not pure metallic Pd.[56] However, after being purified and aged in ambient conditions for 1 h, the as-prepared β-PdH_x nanocrystals were completely converted into Pd. The hydride formation is thus considered as a key factor to determine the formation of the tetrapod nanocrystals.

Reduction of the CO Coverage on Pd(111) by Hydride Formation. In order to investigate how the hydride formation influences the growth of the nanocrystals, we further carried out periodic DFT calculations to compare the chemisorption of CO on Pd(111) and PdH(111) in three different CO adsorption patterns [i.e., $\sqrt{3} \times \sqrt{3}$ R30° (0.33 ML), C(4 × 2)-2CO (0.50 ML), and C(2 × 2)-3CO (0.75 ML)] (Figure 5a–c for models). For all these structures, the average CO adsorption energies are significantly reduced by 0.3–0.5 eV (Table 1) when PdH is formed. This is reasonable as the bare Pd(111) surface is partially saturated by the interstitial H atom, thus weakening the interaction between Pd surface and CO.

The temperature effect has also been considered in our calculations. As shown in Figure 5d,e, surface free energies (φ_{surf}) of CO covered Pd(111) and PdH(111) are both increased, and the high coverage adsorption patterns will gradually convert into low coverage one with the increase of the temperature. Interestingly, the adsorption behavior of PdH(111) surface is rather different from that of Pd(111), especially at relatively high temperature. Above 330 K, C(4 ×

dx.doi.org/10.1021/ja3006429 | J. Am. Chem. Soc. 2012, 134, 7073–7080

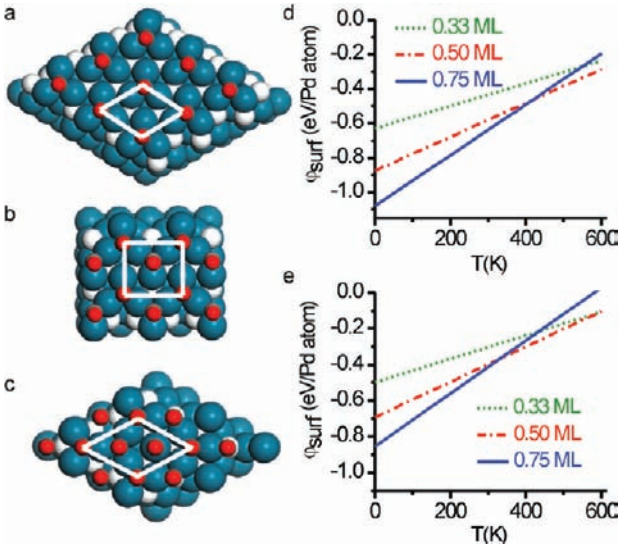

Figure 5. The three CO adsorption patterns on PdH(111): (a) $\sqrt{3} \times \sqrt{3}$ R30° (0.33 ML), (b) C(4 × 2)-2CO (0.50 ML), and (c) C(2 × 2)-3CO (0.75 ML). Dark-cyan balls, Pd; white balls, H; red balls, O; and gray balls, C. Surface free energies (φ_{surf}) of (d) Pd(111)-CO and (e) PdH(111)-CO as a function of temperature for different CO coverages (i.e., 0.33, 0.50, and 0.75 ML).

Table 1. Calculated C−O Distances (d_{C-O}) and Average CO Adsorption Energies ($\overline{\Delta E_{ads}}$) on Pd(111) and PdH(111) at Different Coverages

facets	coverage	($\sqrt{3} \times \sqrt{3}$ R30°)-CO, θ = 0.33 ML, hollow hcp	C(4 × 2)-2CO, θ = 0.50 ML, fcc + hcp	C(2 × 2)-3CO, θ = 0.75 ML, top + fcc + hcp
Pd(111)	d_{C-O} (Å)	1.188	1.182(f), 1.181(h)	1.151(t), 1.183(f), 1.182(h)
		1.189[a]	1.182(f), 1.182(h)[a]	1.151(t), 1.183(f), 1.182(h)[a]
	$\overline{\Delta E_{ads}}$ (eV)	−1.89	−1.75	−1.44
		−2.01[a]	−1.85[a]	−1.46[a]
PdH(111)	d_{C-O} (Å)	1.180	1.179(f), 1.180(h)	1.151(t), 1.180(f), 1.182(h)
	$\overline{\Delta E_{ads}}$ (eV)	−1.50	−1.39	−1.14

[a]Data from ref 34.

2)-2CO becomes more stable than C(2 × 2)-3CO on PdH(111) surface, while C(2 × 2)-3CO is still dominant among the three adsorption structures on Pd(111) until 420 K. According to the Boltzmann distribution, we can estimate the relative concentration of different coverages at different temperatures (Table S1, Supporting Information). At 100 °C, our calculations demonstrated that on PdH(111), there exists 6.5% [$\sqrt{3} \times \sqrt{3}$ R30°, 0.33 ML] + 62.0% [C(4 × 2)-2CO, 0.50 ML] + 31.5% [C(2 × 2)-3CO, 0.75 ML]; while on Pd(111), the relative ratios are 0.7%, 33.7%, and 65.6%, respectively. The high CO coverage on Pd(111) makes it very difficult to have freshly reduced Pd atoms deposited on (111) surfaces and explains why ultrathin nanosheets were yielded in pure CO. On the other hand, for PdH(111) surface, low CO coverage (i.e., 0.33 and 0.50 ML) can also be energetically competitive with those high coverages (i.e., 0.75 ML), providing a chance for Pd atoms to be directly deposited on PdH (111) surfaces. The allowed deposition of Pd atoms on CO-protected PdH (111) surfaces makes it possible to yield the more thermodynamically stable tetrapod structure with lower surface-to-volume ratio than nanosheets.

Our FT-IR measurements (Figure S5, Supporting Information) on the freshly prepared tetrapod nanocrystals revealed that CO adsorbed on the nanocrystals displayed only a characteristic C−O stretching band near 1920 cm^{-1} that can be assigned to CO bound on fcc or hcp 3-fold hollow sites. In contrast, in addition to the C−O stretching band at ∼1920 cm^{-1}, the Pd nanosheets obtained in the presence of pure CO displayed C−O stretching bands at ∼2083 cm^{-1}. In surface science, many studies have demonstrated that high coverage of CO (above 0.6 ML) on Pd(111) would give rise to the presence of linear (atop) CO having a C−O stretching band above 2000 cm^{-1}.[57−59] The absence of C−O stretching band corresponding to atop CO further confirms the relatively low coverage of CO on the surface of tetrapod nanocrystals as predicted by our DFT calculations.

To experimentally demonstrate that Pd atoms can directly deposit on CO-capped Pd(111) in the presence of H_2, uniform 1.8 nm-thick Pd nanosheets with an average edge size of 35 nm were first prepared in pure CO and used as seeds for the further growth studies (Figure S6, Supporting Information). Larger Pd nanosheets (edge size 51 nm), without increasing their thickness (1.8 nm), were readily prepared from small nanosheets (edge size 35 nm) in CO, further confirming that freshly reduced Pd atoms did not deposit on the Pd(111) highly covered by CO. In the copresence H_2 and CO, however, the seeded growth of the small nanosheets produced nanosheets with a thickness increased to ∼3.2 nm. The increased thickness of the nanosheets was a result of the deposition of Pd atoms on Pd(111) surface allowed by the presence of H_2. However, it should be noted that the formation of tetrahedral or tetrapod nanocrystals was also observed in the seeded growth of the small nanosheets in the copresence of H_2 and CO. Both tetrapod and tetrahedral nanocrystals have {111} as their exposure surfaces. As discussed above, the allowed deposition of Pd atoms on CO-capped Pd(111) was mainly due to the lowered CO coverage by PdH_x formation. Following this mechanism, the production of pure Pd tetrahedra would be expected when the CO coverage on Pd(111) could be further reduced during the synthesis. Indeed, when the reaction temperature was increased to 140 °C, we did obtain Pd tetrahedra in the copresence of CO and H_2 (Figure 6).

Optical Properties of Pd Tetrapod Nanocrystals. In the copresence of CO and H_2, the freshly prepared nanocrystals were CO-capped PdH_x but not pure metallic Pd nanocrystals. To investigate the hydrogen releasing from PdH_x tetrapods,

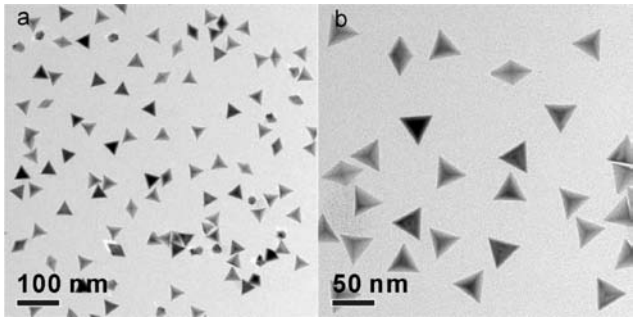

Figure 6. TEM images of the Pd tetrahedral nanocrystals synthesized at 140 °C in the presence of 1:4 CO/H_2.

dx.doi.org/10.1021/ja3006429 | J. Am. Chem. Soc. 2012, 134, 7073−7080

UV−vis NIR spectra of freshly prepared PdH_x tetrapod nanocrystals were monitored. As shown in Figure 7a, the

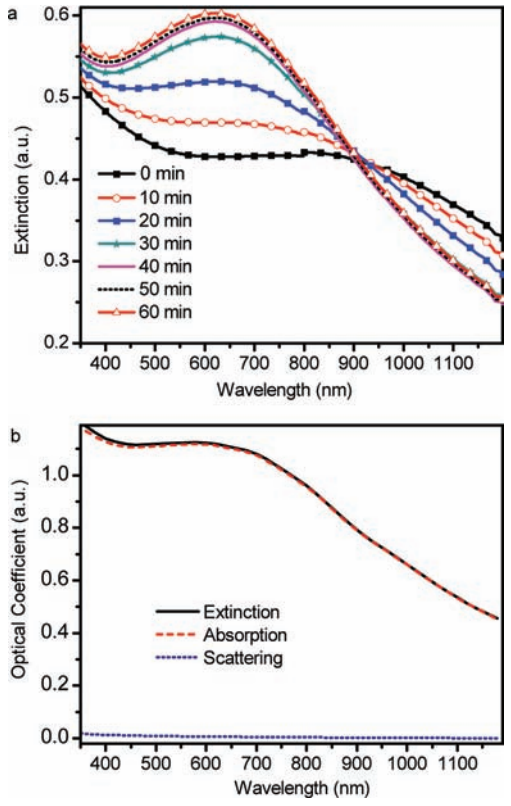

Figure 7. (a) UV−vis NIR spectra of the as-prepared PdH_x tetrapod nanocrystals upon aging in ethanol for different times. (b) The calculated extinction, absorption, and scattering coefficients of Pd tetrapod nanocrystals using the DDA method.

freshly prepared PdH_x tetrapods display a broad absorption peak centered at ~810 nm. Aging the ethanol solution of the PdH_x tetrapods results in the appearance of an absorption peak at ~620 nm.

According to our discrete dipole approximation (DDA) calculations,[60] the peak at 620 nm can be attributed to surface plasmon resonance (SPR) of metallic Pd tetrapods. In our DDA calculations, the dielectric constant of palladium is directly taken from the experimental data by P. B. Johnson and R. W. Christy.[61] As illustrated in Figure 7b, the calculated orientation-averaged extinction spectrum for Pd tetrapods dispersed in ethanol medium (n = 1.36) shows a broad extinction peak at ~610 nm. It should also be noted that the significant contribution to the extinction spectrum of Pd tetrapods is caused by absorption, and the scattering coefficient is negligibly small. It is well-known that the LSPR modes of Pd nanospheres are typically located in the UV region. For example, the SPR peak of a Pd nanosphere with a diameter of 60 nm is calculated at ~340 nm. However, in a tetrapod nanocrystal with a side length of 60 nm (tip-to-tip distance), the symmetry breaking results in a red-shifted and broader LSPR peak at ~610 nm. From the experimental results and theoretical analysis, it is predicted that the LSPR modes can be controlled through the whole visible region, even in the near-infrared region, if the shape of Pd nanoparticles are well designed.

Shape-Dependent Conversion of PdH_x Nanocrystals. It should be noted that the red-shift of SPR peaks after hydrogen adsorption were also previously reported on supported Pd nanodisks.[62] Before 30 min, the intensity of the SPR peak of the Pd tetrapods at 620 nm increases linearly, indicating a continuous and sustained release of hydrogen from the as-prepared PdH_x tetrapod nanocrystals within 30 min. After 30 min, the hydrogen release is much slower and becomes negligible beyond 60 min. As revealed by XRD measurements (Figure S7, Supporting Information), the hydrogen release kinetics from PdH_x nanocrystals is shape-dependent. The conversion of hydride was characterized by the fraction of the Pd(111) diffraction peak over the sum of those PdH_x(111) and Pd(111). Upon aging in air, as shown in Figure 8a, the

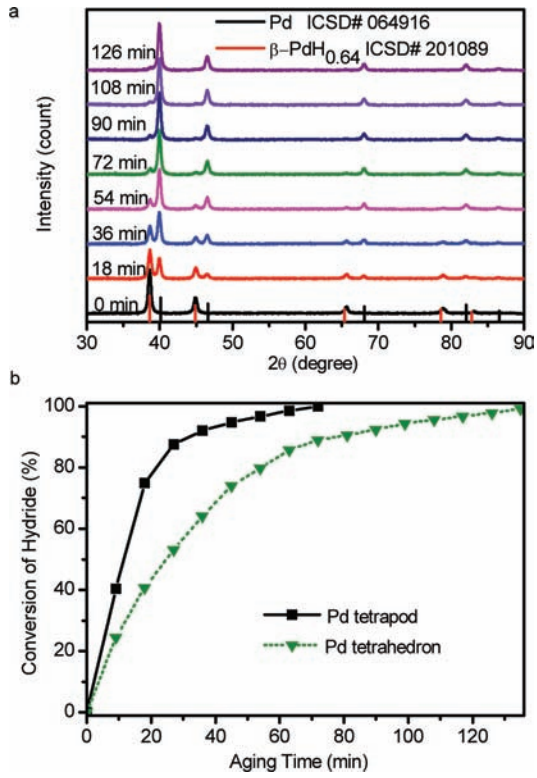

Figure 8. (a) XRD of Pd tetrahedral nanocrystals. (b) Conversion of PdH_x tetrahedron and tetrapod nanocrystals upon aging in air as characterized by time-domain XRD measurements.

conversion rate of the fresh PdH_x tetrahedral nanocrystals prepared at 140 °C into pure Pd is much slower than the tetrapods (Figure 8b). The much faster hydrogen releasing kinetics from tetrapod nanocrystals than from tetrahedral nanocrystals can be explained by the presence of more edge and tip sites in the Pd tetrapods.

Electrocatalysis and Catalysis by the Pd Tetrapod Nanocrystals. The electrocatalysis performances of as-obtained tetrapod Pd nanocrystals were studied by the oxidation of formic acid. The commercial Pd black catalyst was used as the reference for comparison. The ECSA of the as-prepared Pd tetrapods was measured to be 15.9 m^2/g, which is 45.6% of the commercial Pd black catalyst (34.9 m^2/g) (Figure S8, Supporting Information). The ECSA of Pd tetrapods is 60.7% of the theoretical maximum surface area (26.2 m^2/g) calculated from an ideal tetrapod geometry, suggesting that the as-prepared Pd tetrapods have a rather clean surface. Figure 9a

dx.doi.org/10.1021/ja3006429 | J. Am. Chem. Soc. 2012, 134, 7073−7080

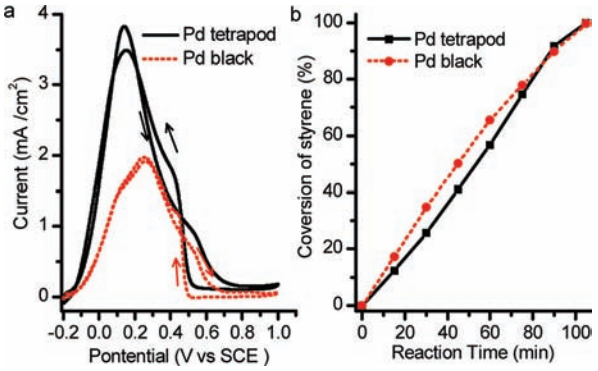

Figure 9. (a) Comparison of electrocatalytic properties of the Pd tetrapods and Pd black in the oxidation of formic acid. The CV curves were recorded in an aqueous solution containing 0.5 M H_2SO_4 and 0.25 M HCOOH at a scan rate of 50 mV/s. (b) Comparison of catalytic properties of the Pd tetrapods and Pd black in the hydrogenation of styrene. Catalysis conditions: 0.5 mg of Pd catalyst and 20 mmol styrene in 10 mL of ethanol under 2 bar H_2 at 40 °C.

compares the CV curves for the electro-oxidations of formic acid on both catalysts. For straightforward comparison of the surface activity, the current densities were normalized to ECSAs. The maximum current density by the Pd tetrapods is 3.84 mA/cm^2, twice of that by the Pd black catalyst (1.92 mA/cm^2). Moreover, the Pd tetrapods have a lower peak potential at 0.140 V (vs SCE) than the Pd black (0.276 V vs SCE), which can be attributed to the presence of mainly Pd(111) facets in the tetrapod nanocrystals.[63] The Pd tetrapod nanocrystals also displayed better stability during the electrochemical measurements (Figures S9, Supporting Information). After repetitive 100 CV scans between −0.2 and 0.8 V (vs SCE), the peak current density of the Pd tetrapods was reduced by 9%. In comparison, a 26% drop in the electrocatalysis activity was observed on the commercial Pd black.

In addition to their excellent electrocatalysis in the oxidation of formic acid, the as-prepared Pd tetrapods exhibit high catalytic performance in the hydrogenation of styrene without the need to do any pretreatment. As shown in Figure 9b, the Pd tetrapods show a comparable catalytic activity to the commercial Pd black catalyst containing the same weight of Pd. A full conversion of styrene was achieved by both catalysts in 105 min at 40 °C. But it is worth noting that although the Pd black showed a slightly better performance in the first 30 min, its catalytic activity was decreasing with the proceeding of the reaction. But instead of a decrease, a slight increase of the catalytic activity was even observed from the Pd tetrapod nanocrystals during the catalysis. Considering the Pd tetrapods have a smaller surface area than the Pd black, the TOF for the surface atoms on the Pd tetrapods is essentially much higher than that on the Pd black catalyst. Based on the conversion at 90 min, the turnover frequencies of the surface atoms (calculated from ECSAs) on the Pd tetrapods and the Pd black were estimated to be 92 700 and 41 600 h^{-1}, respectively.

CONCLUSION

In conclusion, single-crystalline tetrapod Pd nanocrystals with uniform diameter were successfully prepared in the presence of hydrogen and carbon monoxide mixture. The as-made Pd tetrapod nanocrystals are bound with {111} facets. Studies revealed that the freshly obtained tetrapod nanocrystals were β-PdH_x nanocrystals and gradually transformed into pure Pd nanocrystals in air. Through DFT calculations, the formation of palladium hydride during synthesis was found essential to manipulate CO coverage on Pd to obtain the tetrapod nanocrystals. Together with the use of specific strong adsorbates to control the surface structure of Pd nanocrystals, the shape-control strategy reported here could provide a new synthetic avenue to further enrich the shape of Pd nanocrystals.

ASSOCIATED CONTENT

Supporting Information

Additional characterization data. This material is available free of charge via the Internet at http://pubs.acs.org.

AUTHOR INFORMATION

Corresponding Author

nfzheng@xmu.edu.cn; gfu@xmu.edu.cn

Notes

The authors declare no competing financial interest.

ACKNOWLEDGMENTS

We thank the MOST of China (2011CB932403, 2009CB930703), the NSFC (21131005, 21021061, 20925103, 20973139, 21133004), the Fok Ying Tung Education Foundation (121011), and the Fundamental Research Funds for the Central Universities for financial support.

REFERENCES

(1) Sau, T. K.; Rogach, A. L.; Jackel, F.; Klar, T. A.; Feldmann, J. *Adv. Mater.* **2010**, *22*, 1805.
(2) Tao, A. R.; Habas, S.; Yang, P. *Small* **2008**, *4*, 310.
(3) Xia, Y. N.; Xiong, Y. J.; Lim, B.; Skrabalak, S. E. *Angew. Chem., Int. Ed.* **2009**, *48*, 60.
(4) Sau, T. K.; Rogach, A. L. *Adv. Mater.* **2010**, *22*, 1781.
(5) Peng, Z. M.; Yang, H. *Nano Today* **2009**, *4*, 143.
(6) Chen, M.; Wu, B.; Yang, J.; Zheng, N. *Adv. Mater.* **2012**, *24*, 862.
(7) Habas, S. E.; Lee, H.; Radmilovic, V.; Somorjai, G. A.; Yang, P. *Nat. Mater.* **2007**, *6*, 692.
(8) Song, H.; Kim, F.; Connor, S.; Somorjai, G. A.; Yang, P. D. *J. Phys. Chem. B* **2005**, *109*, 188.
(9) Xiong, Y. J.; Cai, H. G.; Wiley, B. J.; Wang, J. G.; Kim, M. J.; Xia, Y. N. *J. Am. Chem. Soc.* **2007**, *129*, 3665.
(10) Huang, X.; Zhang, H.; Guo, C.; Zhou, Z.; Zheng, N. *Angew. Chem., Int. Ed.* **2009**, *48*, 4808.
(11) Wu, B.; Zheng, N.; Fu, G. *Chem. Commun.* **2011**, *47*, 1039.
(12) Huang, X.; Tang, S.; Mu, X.; Dai, Y.; Chen, G.; Zhou, Z.; Ruan, F.; Yang, Z.; Zheng, N. *Nat. Nanotechnol.* **2011**, *6*, 28.
(13) Chen, G.; Tan, Y.; Wu, B.; Fu, G.; Zheng, N. *Chem. Commun.* **2012**, *48*, 2758.
(14) Huang, X.; Zhao, Z.; Fan, J.; Tan, Y.; Zheng, N. *J. Am. Chem. Soc.* **2011**, *133*, 4718.
(15) Huang, X.; Tang, S.; Zhang, H.; Zhou, Z.; Zheng, N. *J. Am. Chem. Soc.* **2009**, *131*, 13916.
(16) Huang, X.; Tang, S.; Yang, J.; Tan, Y.; Zheng, N. *J. Am. Chem. Soc.* **2011**, *133*, 15946.
(17) Zhou, Z. Y.; Tian, N.; Li, J. T.; Broadwell, I.; Sun, S. G. *Chem. Soc. Rev.* **2011**, *40*, 4167.
(18) Astruc, D.; Lu, F.; Aranzaes, J. R. *Angew. Chem., Int. Ed.* **2005**, *44*, 7852.
(19) Narayanan, R.; El-Sayed, M. A. *J. Phys. Chem. B* **2005**, *109*, 12663.
(20) Eustis, S.; El-Sayed, M. A. *Chem. Soc. Rev.* **2006**, *35*, 209.
(21) Xia, Y.; Halas, N. J. *MRS Bull.* **2005**, *30*, 338.
(22) Anker, J. N.; Hall, W. P.; Lyandres, O.; Shah, N. C.; Zhao, J.; Van, D. R. P. *Nat. Mater.* **2008**, *7*, 442.

(23) Jain, P. K.; Huang, X.; El-Sayed, I. H.; El-Sayed, M. A. *Acc. Chem. Res.* **2008**, *41*, 1578.
(24) Liz-Marzan, L. M. *Langmuir* **2006**, *22*, 32.
(25) Huang, X.; Zheng, N. *J. Am. Chem. Soc.* **2009**, *131*, 4602.
(26) Rand, D. A. J.; Woods, R. *J. Electroanal. Chem.* **1972**, *35*, 209.
(27) Kresse, G.; Hafner, J. *Phys. Rev. B* **1993**, *48*, 13115.
(28) Kresse, G.; Furthmüller, J. *Phys. Rev. B* **1996**, *54*, 11169.
(29) Perdew, J. P.; Burke, K.; Ernzerhof, M. *Phys. Rev. Lett.* **1996**, *77*, 3865.
(30) Blöchl, P. E. *Phys. Rev. B* **1994**, *50*, 17953.
(31) Kresse, G.; Joubert, D. *Phys. Rev. B* **1999**, *59*, 1758.
(32) Tüshaus, M.; Berndt, W.; Conrad, H.; Bradshaw, A. M.; Persson, B. *Appl. Phys. A: Mater. Sci. Process.* **1990**, *51*, 91.
(33) Rose, M. K.; Mitsui, T.; Dunphy, J.; Borg, A.; Ogletree, D. F.; Salmeron, M.; Sautet, P. *Surf. Sci.* **2002**, *512*, 48.
(34) Loffreda, D.; Simon, D.; Sautet, P. *Surf. Sci.* **1999**, *425*, 68.
(35) Sautet, P.; Rose, M. K.; Dunphy, J. C.; Behler, S.; Salmeron, M. *Surf. Sci.* **2000**, *453*, 25.
(36) Yudanov, I. V.; Sahnoun, R.; Neyman, K. M.; Rösch, N.; Hoffmann, J.; Schauermann, S.; Johánek, V.; Unterhalt, H.; Rupprechter, G.; Libuda, J.; Freund, H.-J. *J. Phys. Chem. B* **2003**, *107*, 255.
(37) Morkel, M.; Rupprechter, G.; Freund, H.-J. *Surf. Sci.* **2005**, *588*, L209.
(38) Morkel, M.; Rupprechter, G.; Freund, H.-J. *J. Chem. Phys.* **2003**, *119*, 10853.
(39) Rupprechter, G.; Morkel, M.; Freund, H.-J.; Hirschl, R. *Surf. Sci.* **2004**, *554*, 43.
(40) Cerdá, J. I.; Santos, B.; Herranz, T.; Puerta, J. M.; de la Figuera, J.; McCarty, K. F. *J. Phys. Chem. Lett.* **2011**, *3*, 87.
(41) Worsham, J. E., Jr.; Wilkinson, M. K.; Shull, C. G. *J. Phys. Chem. Solids* **1957**, *3*, 303.
(42) Drexel, W.; Murani, A.; Tocchetti, D.; Kley, W.; Sosnowska, I.; Ross, D. K. *J. Phys. Chem. Solids* **1976**, *37*, 1135.
(43) Añez, R.; Sierraalta, A.; Martorell, G.; Sautet, P. *Surf. Sci.* **2009**, *603*, 2526.
(44) Hofmann, A.; Sauer, J. *J. Phys. Chem. B* **2004**, *108*, 14652.
(45) Frisch, M. J.; Trucks, G. W.; Schlegel, H. B.; Scuseria, G. E.; Robb, M. A.; Cheeseman, J. R.; Montgomery, J. A., Jr.; Vreven, T.; Kudin, K. N.; Burant, J. C.; Millam, J. M.; Iyengar, S. S.; Tomasi, J.; Barone, V.; Mennucci, B.; Cossi, M.; Scalmani, G.; Rega, N.; Petersson, G. A.; Nakatsuji, H.; Hada, M.; Ehara, M.; Toyota, K.; Fukuda, R.; Hasegawa, J.; Ishida, M.; Nakajima, T.; Honda, Y.; Kitao, O.; Nakai, H.; Klene, M.; Li, X.; Knox, J. E.; Hratchian, H. P.; Cross, J. B.; Bakken, V.; Adamo, C.; Jaramillo, J.; Gomperts, R.; Stratmann, R. E.; Yazyev, O.; Austin, A. J.; Cammi, R.; Pomelli, C.; Ochterski, J. W.; Ayala, P. Y.; Morokuma, K.; Voth, G. A.; Salvador, P.; Dannenberg, J. J.; Zakrzewski, V. G.; Dapprich, S.; Daniels, A. D.; Strain, M. C.; Farkas, O.; Malick, D. K.; Rabuck, A. D.; Raghavachari, K.; Foresman, J. B.; Ortiz, J. V.; Cui, Q.; Baboul, A. G.; Clifford, S.; Cioslowski, J.; Stefanov, B. B.; Liu, G.; Liashenko, A.; Piskorz, P.; Komaromi, I.; Martin, R. L.; Fox, D. J.; Keith, T.; Al-Laham, M. A.; Peng, C. Y.; Nanayakkara, A.; Challacombe, M.; Gill, P. M. W.; Johnson, B.; Chen, W.; Wong, M. W.; Gonzalez, C.; Pople, J. A. *Gaussian 03*, revision D.01; Gaussian, Inc.: Wallingford, CT, 2004.
(46) Woon, D. E.; Dunning, J. T. H. *J. Chem. Phys.* **1995**, *103*, 4572.
(47) Hara, M.; Linke, U.; Wandlowski, T. *Electrochim. Acta* **2007**, *52*, 5733.
(48) Manna, L.; Scher, E. C.; Alivisatos, A. P. *J. Am. Chem. Soc.* **2000**, *122*, 12700.
(49) Peng, X. *Adv. Mater.* **2003**, *15*, 459.
(50) Wang, D.; Lieber, C. M. *Nat. Mater.* **2003**, *2*, 355.
(51) Newton, M. C.; Warburton, P. A. *Mater. Today* **2007**, *10*, 50.
(52) Chen, S.; Wang, Z. L.; Ballato, J.; Foulger, S. H.; Carroll, D. L. *J. Am. Chem. Soc.* **2003**, *125*, 16186.
(53) Palczewska, W. *Adv. Catal.* **1975**, *24*, 245.
(54) Goltsova, M. V. *Int. J. Hydrogen Energy* **2006**, *31*, 223.
(55) Jewell, L. L.; Davis, B. H. *Appl. Catal., A* **2006**, *310*, 1.
(56) Schirber, J. E.; Morosin, B. *Phys. Rev. B* **1975**, *12*, 117.
(57) Kaichev, V. V.; Prosvirin, I. P.; Bukhtiyarov, V. I.; Unterhalt, H.; Rupprechter, G.; Freund, H.-J. *J. Phys. Chem. B* **2003**, *107*, 3522.
(58) Unterhalt, H.; Rupprechter, G.; Freund, H.-J. *J. Phys. Chem. B* **2002**, *106*, 356.
(59) Szanyi, J.; Kuhn, W. K.; Goodman, D. W. *J. Vac. Sci. Technol., A* **1993**, *11*, 1969.
(60) Draine, B. T.; Flatau, P. J. *J. Opt. Soc. Am. A* **1994**, *11*, 1491.
(61) Johnson, P.; Christy, R. *Phys. Rev. B.* **1974**, *9*, 5056.
(62) Langhammer, C.; Zoric, I.; Kasemo, B.; Clemens, B. M. *Nano Lett.* **2007**, *7*, 3122.
(63) Baldauf, M.; Kolb, D. M. *J. Phys. Chem.* **1996**, *100*, 11375.